

Catalysts

Large Ferrierite Crystals as Models for Catalyst Deactivation during Skeletal Isomerisation of Oleic Acid: Evidence for Pore Mouth Catalysis

Sophie C. C. Wiedemann,^[a, b] Zoran Ristanović,^[a] Gareth T. Whiting,^[a] V. R. Reddy Marthala,^[c] Jörg Kärgner,^[d] Jens Weitkamp,^[c] Bas Wels,^[b] Pieter C. A. Bruijninx,^[a] and Bert M. Weckhuysen^{*[a]}

Abstract: Large zeolite crystals of ferrierite have been used to study the deactivation, at the single particle level, of the alkyl isomerisation catalysis of oleic acid and elaidic acid by a combination of visible micro-spectroscopy and fluorescence microscopy (both polarised wide-field and confocal modes). The large crystals did show the desired activity, albeit only traces of the isomerisation product were obtained and low conversions were achieved compared to commercial ferrierite powders. This limited activity is in line with their lower external non-basal surface area, supporting

the hypothesis of pore mouth catalysis. Further evidence for the latter comes from visible micro-spectroscopy, which shows that the accumulation of aromatic species is limited to the crystal edges, while fluorescence microscopy strongly suggests the presence of polyenylic carbocations. Light polarisation associated with the spatial resolution of fluorescence microscopy reveals that these carbonaceous deposits are aligned only in the larger 10-MR channels of ferrierite at all crystal edges. The reaction is hence further limited to these specific pore mouths.

Introduction

Shape selectivity of zeolite-based materials is considered to originate from their well-defined internal microstructure,^[1] for example where potential bulky transition states or intermediate species are inhibited by the size of the channels (or their intersections) and cages around the active sites. Nonetheless, the external surface may in some cases also play an important role in the selectivity towards a particular isomer or product,^[2] and in the past decades a number of mechanisms have been proposed to explain non-statistical product distributions based on specific features of the outer surface of the zeolite crystal.^[3]

For example, the methyl-branching pattern observed in the hydroisomerisation of long chain *n*-alkanes (> C7) with one-dimensional medium-pore zeolites (e.g., of framework topologies MTT^[4] and TON^[5]) has been attributed to pore mouth and key-lock catalysis.^[6–10] The former assumes entry of the molecule to optimise the van der Waals interactions with the channel atoms; subsequently, branching occurs preferentially at acid sites located within the pore mouth in order to ease desorption, and the molecules show a unimodal distribution of the methyl-branching, close to the chain end. In the key-lock configuration, both the length and polarity of the carbon chain allow it to enter by its extremities in two adjacent pores, resulting in a bimodal distribution of methyl-branching. However, the relative importance of the different catalytic models applied to this reaction has, since their initial introduction, been the subject of debate.^[11,12] Enthalpic and entropic considerations, for instance, suggest that they apply only in the case of an inaccessible internal structure, or in zeolites with small-membered ring channels.^[13]

Pore mouth catalysis has also been postulated as an explanation for the increase in selectivity shown by protonated ferrierite (H-FER) at longer time-on-stream (TOS) in the butene to isobutene alkyl isomerisation.^[14–17] Here, the concept of pore mouth catalysis is limited to the location of reaction at the extremities of the pores, since steric factors in the approach to the channel are less important with such small molecules. In this medium-pore zeolite, the 10-membered ring (10-MR) channels (4.2×5.4 Å) are perpendicularly crossed with the 8-MR channels (3.4×4.7 Å). The improvement of the isobutene se-

[a] S. C. C. Wiedemann, Z. Ristanović, Dr. G. T. Whiting, Dr. P. C. A. Bruijninx, Prof. Dr. B. M. Weckhuysen
Inorganic Chemistry and Catalysis
Debye Institute for Nanomaterials Science, Utrecht University
Universiteitsweg 99, 3584 CG Utrecht (The Netherlands)
E-mail: b.m.weckhuysen@uu.nl

[b] S. C. C. Wiedemann, Dr. B. Wels
Croda Nederland B.V., Buurtje 1, 2800 BE Gouda (The Netherlands)

[c] Dr. V. R. Reddy Marthala, Prof. Dr. J. Weitkamp
Institute of Chemical Technology, University of Stuttgart
Pfaffenwaldring 55, 70569 Stuttgart (Germany)

[d] Prof. Dr. J. Kärgner
Department of Interface Physics, University of Leipzig
Linnéstrasse 5, 04103 Leipzig (Germany)

© 2015 The Authors. Published by Wiley-VCH Verlag GmbH & Co. KGaA. This is an open access article under the terms of Creative Commons Attribution NonCommercial License, which permits use, distribution and reproduction in any medium, provided the original work is properly cited and is not used for commercial purposes.

lectivity, resulting from the decrease in cracking reactions, correlates with build-up of hydrocarbon deposits in the pore system.^[14,15] The filling of the volume of the H-FER zeolite crystal by slowly diffusing carbonaceous species,^[16] the beneficial influence of the pore mouth ellipticity as well as the improved isomerisation activity observed with smaller crystallites^[17] have all been listed as experimental evidence for the concept of pore mouth catalysis.

Recently, the pore mouth catalysis model has also been proposed for the liquid-phase skeletal isomerisation of oleic acid (OA, mainly *cis*-9-octadecenoic acid) in the presence of H-FER at 260 °C (Figure 1).^[18] Despite very early pore blockage, high OA conversion and selectivity to branched-chain unsaturated fatty acids (BUFA) have been reported; the high conversion may be explained by catalysis on the external surface, however the high selectivity suggests a constrained active site with shape-selective features, such as pockets or pore mouths. The latter proposal is further substantiated by the observation that the selectivity to BUFA over oligomerisation is enhanced by the introduction of a bulky Lewis base, such as triphenylphosphine (TPP).^[19] It is believed that such a promoter compound binds with any active sites at the external surface, eliminating residual non-shape-selective reactions there.

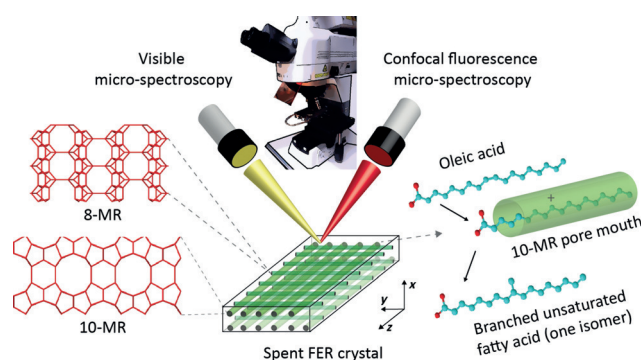


Figure 1. Skeletal isomerisation of OA in the presence of protonated zeolite ferrierite (H-FER). The right side of the Figure illustrates the concept of pore mouth catalysis, postulated to control the selectivity of this catalytic reaction, while the left shows a schematic representation of the spent H-FER crystal analysis by visible and confocal micro-spectroscopy.

Pore blockage could be correlated with an increase in carbonaceous deposits formed in the spent catalyst powder. Long-chain alkyl benzenes were identified as the major coke-like constituents.^[18] In addition, catalyst deactivation has been found to worsen by the poisoning of the pore mouth acid sites due to the formation of enylic carbocations.^[18] Extensive characterisation of the catalyst with bulk analytical techniques provided many insights into the mechanisms of deactivation and the extent to which the pore mouths are involved in the isomerisation reaction.

To add to the complexity of this chain-branching reaction, geometric and positional isomerisation of the OA double bond occur under the applied reaction conditions. The *cis/trans* isomerisation has an activation energy of about 125 kJ mol⁻¹, and is known to occur during physical refining of vegetable oils

above 250 °C.^[20] Strong (Lewis or Brønsted) acids also catalyse geometric isomerisation at much lower reaction temperatures.^[21] In the alkyl isomerisation of OA using H-FER, a significant amount of the *trans*-isomer elaidic acid (EA, *trans*-9-octadecenoic acid) is indeed formed well before reaching reaction temperature, resulting in a solid crude mixture at low conversion.^[18] γ -Lactones are also observed in the reaction mixture, confirming that the zeolite material also catalyses positional isomerisation of the double bond.^[18] These side reactions are therefore to be included in an investigation of the catalysis at the molecular level. In particular, the configuration of the double bond seems to be a key parameter in the catalytic mechanism as it determines the interaction with the acid sites of the pore mouth.

Various micro-spectroscopy methods,^[22] including scanning transmission X-ray microscopy,^[23] coherent *anti*-Stokes Raman micro-spectroscopy,^[24] confocal fluorescence microscopy,^[25,26] UV/Vis/NIR micro-spectroscopy^[27] and IR micro-spectroscopy,^[28–30] have been used extensively in recent years to study the spatiotemporal formation of hydrocarbons in the crystals of various zeolites and zeotypes, including ones with MFI, CHA, FER and BEA topologies.^[31–36] This multi-technique approach has also been successfully applied to the study of spatiotemporal heterogeneities in for example, individual fluid catalytic cracking catalyst particles of different age,^[37] or catalyst powder before/after steaming.^[38–40] UV/Vis and IR micro-spectroscopies are limited in spatial resolution, but have proven to be valuable tools for the chemical identification of hydrocarbon deposits; confocal fluorescence microscopy on the other hand enables their 3D visualisation with a resolution down to approximately 500 nm. In addition, measurements based on visible absorption with polarised light,^[41] or the study of the polarisation of emitted fluorescent light,^[42] can be used to reveal the location and specific orientation in the zeolite framework of the chromophore under investigation, and link their formation and presence to specific channel types. This powerful use of polarised light in combination with micro-spectroscopy has also been applied to coke molecules, carbocations and their precursors which, due to their elongated structures, have a clearly oriented dipole moment vector.^[32,33] It should be noted that large zeolite crystals are typically used as catalyst materials for investigations with the techniques listed above, as dictated by their spatial resolution.

It was anticipated that the micro-spectroscopic, multi-technique approach can be equally useful to the investigation of deactivation during the OA alkyl chain isomerisation reaction; the main “coke” components (i.e., long chain alkylbenzenes and enylic carbocations) can be detected by the above-mentioned characterisation techniques. The synthesis of the large H-FER crystals required for such studies has been reported in the literature^[43,44] and these model catalysts have been used in a number of fundamental diffusion studies.^[45–47]

In this work, we build on our recent results on ferrierite deactivation obtained with bulk characterisation techniques^[18,49] and study the deactivation of H-FER during the skeletal isomerisation of OA using large zeolite crystals as model catalysts, in order to seek additional evidence supporting the concept of

Symbol	Name	Origin	Crystal size [μm]	Supplied form	Nominal Si/Al	Activation method
powder 1 ^[b]	HSZ720KOA	tosoh	0.3–0.5	K^+	8.5 ^[a]	wet exchange
powder 2	CP914	zeolyst	≈ 1	NH_4^+	27 ^[a]	calcination
crystals	B3 in ref. [46]	[18]	> 150	Na^+/H^+	23	wet exchange/ calcination

[a] Commercial values. [b] Same batch of powder 1 as used in ref. [18].

pore mouth catalysis, as illustrated in Figure 1. To further substantiate and confirm this hypothesis at the molecular level, the precise distribution of carbonaceous deposits in individual zeolite crystals has been investigated. Scanning electron microscopy (SEM) confirmed the integrity of the large crystals after catalysis, while visible micro-spectroscopy allowed a comparison of the bulk with local electronic spectra in order to determine the nature of the carbonaceous deposits formed on the large zeolite crystals. Finally, a combination of wide-field and confocal fluorescence microscopy has enabled us, together with polarisation-dependent laser light excitation, to determine the 3D location of the carbonaceous deposits on a number of ferrierite crystals. The different carbonaceous species were found to be located at all edges of the 10-MR channels of the large H-FER crystals, and hence at the pore mouths of these channels, providing experimental evidence for the existence of pore mouth catalysis in H-FER materials during the liquid-phase skeletal isomerisation of OA.

Results and Discussion

The model ferrierite catalyst used in this study, further denoted as crystals, consists of large crystals with typical dimensions of $170 \times 70 \times 5 \mu\text{m}$ and has a low concentration of Brønsted acid sites (Si/Al = 23, Table 1). The large size of the zeolite crystallites means that only a relatively small external surface is available. As the alkyl isomerisation is believed to happen within the channel pore mouths,^[18] this low surface area and acidity is expected to severely limit the activity of the model catalyst, precluding a direct comparison with catalyst performance results previously reported for larger scale reactions run with conventional zeolite powders. Therefore, two additional protonated ferrierite reference samples, characterised by small-

er zeolite crystals, have been included in the catalytic testing for comparison; these are annotated as powder 1 (Si/Al = 8.5) with a crystal size below $1 \mu\text{m}$ and powder 2 (Si/Al = 27) with a crystal size around $1 \mu\text{m}$.

Model catalyst morphology

SEM was used to evaluate the morphology of the model crystals after activation, and after post-reaction cleaning (Figure 2). The SEM images confirm that morphology is conserved after the various physical treatments involved in the catalytic activation and testing (respectively shaking, slow swirling and filtration). Two types of zeolite crystals can be discerned; that is, thin platelets and exfoliated platelets. We focused on isolated intact FER crystals; their sizes vary between 3–5 μm (thickness, X), 20–90 μm (width, Y) and 150–200 μm (length, Z). It is important to note that the 10-MR channels run along the length of the model crystals, crossing perpendicular to the 8-MR channels,^[48] as shown in the schematic representation of a flat crystal (Figure 2c). In the case of pore mouth catalysis, the non-basal plane external surface is the relevant parameter in estimating the number of accessible channels for reaction.

Catalytic testing

Together with the blank, the design includes 12 parallel experiments. All catalyst materials have been tested with OA for the alkyl isomerisation, and powder 2 and the crystals additionally with EA. The main results of the catalytic testing are summarised in Table 2.

Despite the very long reaction times, only powder 1 showed (almost) complete OA conversion at 1.0 wt.% loading (96 wt.%, exp. 1). The lower OA conversion recorded for

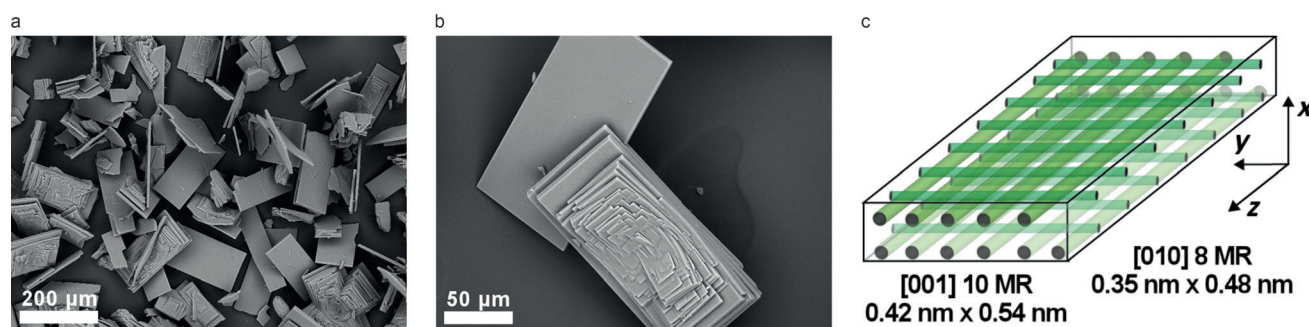


Figure 2. SEM images of typical model crystals: a) after activation, b) after activation and alkyl isomerisation of OA (260 °C, 96.5 h, experiment 7) and post-reaction cleaning; c) the microchannel orientation.^[48]

Table 2. Crude product analysis, for the skeletal isomerisation of OA or EA over various H-FER (1.0 and 2.0 wt.% loading) samples after 96.5 h at 260 °C.

Expt.	Cat.	Cat. loading [wt.%]	Feed type	Oligomer yields [wt.%]	BUFA yields [wt.%]	Lactone yields [wt.%]	Overall conversion [wt.%]	Selectivity to BUFA [wt.%]	EA/(EA + OA) [wt.%]
1	powder 1	1.0	OA	20	56	9.3	96	61	68
2	powder 1	2.0	OA	25	53	9.2	97	57	72
3	powder 2	1.0	OA	14	54	8.1	83	68	66
4	powder 2	2.0	OA	20	60	7.0	96	65	63
5	powder 2	1.0	EA ^[a]	10	7.7	6.0	25	34	56
6	powder 2	1.0	EA	11	65	5.6	89	77	59
7	crystals	1.0	OA	10	ND	traces	12	0	41
8	crystals	1.0	EA ^[a]	10	ND	ND	15	0	81
9	crystals	2.0	EA	11	traces	traces	14	> 0	77
10	blank	/	OA	9	ND	ND	12	0	26
11	blank	/	EA ^[a]	11	ND	ND	14	0	82
12	blank	/	EA	10	ND	ND	12	0	87

[a] Non-distilled EA contains ≈ 100 ppm Na⁺, K⁺. ND = not detected.

powder 2 (83 wt.%, exp. 3) clearly reflects its lower total acidity (Si/Al). As expected, increasing the catalyst loading to 2.0 wt.% resulted in higher conversion (97 wt.% for powder 1 and 96 wt.% for powder 2, respectively; exp. 2 and 4 in Table 2), but at the cost of selectivity to BUFA (e.g., from 68 to 65 wt.% for powder 2). Most of the decrease in BUFA selectivity can be explained by the increase in oligomers, while the amount of lactones formed remains approximatively constant.

Geometric isomerisation of OA is an (acid-catalysed) equilibrium reaction with lower activation energy than the alkyl chain isomerisation, with the *cis/trans* ratio tending to ≈ 0.5 under the given reaction conditions. As the branching reaction takes place at the pore mouth, the geometric configuration of the fatty acid is expected to have an influence on the overall reaction rate. In order to verify this influence, and potentially enhance both conversion and BUFA selectivity, pure EA was also used as substrate (exp. 5 and 6). The commercial EA was unfortunately found to contain significant levels of Na⁺ and K⁺ ions, which are known to limit conversion^[50] by blocking the channels, deactivating the active sites and/or lowering the acidity.^[51] The detrimental effect of these cations was confirmed by a dramatic fall in conversion from 83 to 25 wt.% (exp. 5). When the EA was purified by distillation, activity and selectivity were significantly higher than in the reaction starting from OA under comparable conditions (exp. 6 versus exp. 3), and oligomers and lactones yields were also lower.

The conversion of OA with the crystals at 1.0 wt.% loading (exp. 7) is equivalent to the control (exp. 10), and much lower, under the same conditions, than that of powder 2 of similar acidity. With EA and a 2.0 wt.% catalyst loading (exp. 9), the conversion increases by only 2 wt.%, in contrast to the large increase seen with EA for the smaller ferrierite crystals. The low OA conversion measured with the crystals can be attributed to the much lower (non-basal) external surface area, and thus pore mouth concentration. The very low activity of the crystals is therefore also consistent with the pore mouth catalysis hypothesis.

Importantly, though, the composition of the crude mixtures obtained from the model catalyst with OA or distilled EA (exp. 7 and 9, respectively) clearly differs from those resulting

from the blanks (exp. 10 and 12). For both OA and EA, the crystals are catalysing the *cis/trans* isomerisation towards its equilibrium value, starting from above (EA) and below (OA). Positional isomerisation also takes place over the model crystals, as γ -lactones are also detected (Table 2 and chromatograms shown in Figure 3b for exp. 9 with distilled EA). When starting with non-distilled EA (exp. 8), the few acid sites available for reactions were, as expected, deactivated by the presence of Na⁺, K⁺. Furthermore, in the run with distilled EA and a 2.0 wt.% catalyst loading (exp. 9), BUFA traces could be identified by GC-MS. Detection of these traces required distillation, hydrogenation and methylation of the sample, to ensure adequate chromatographic resolution between branched product and linear feed (Figure 3b). The fact that they are formed, albeit in small amounts, and are not detected at all in the blank runs, shows that model crystals are able to catalyse the desired reaction.

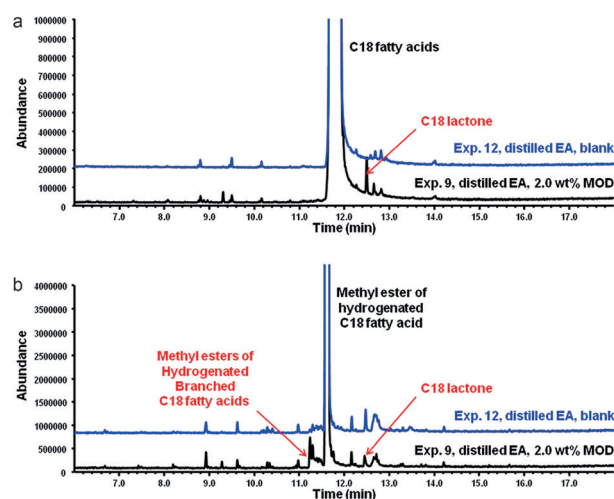


Figure 3. GC-MS total ion chromatogram of distilled product from the alkyl isomerisation (96.5 h at 260 °C) of distilled EA: exp. 12 in the absence of catalyst and exp. 9 in the presence of the model H-FER (2.0 wt.% crystals loading). a) The samples were first analysed without derivatisation. b) The same samples were reanalysed after hydrogenation and methylation, in order to ensure resolution between methylated product and feed.

The higher rate of skeletal isomerisation with EA compared to OA suggests that the *trans* form is favoured for entry into the channels, and this is also intuitively expected as it has a smaller molecular cross-section; such shape-selective sorption has been recently demonstrated in the preferential hydrogenation of methyl esters of EA over OA.^[52] Under our reaction conditions, even weakly acidic sites on the external catalyst surface are able to catalyse the initial isomerisation of OA to EA. However, it is not possible to determine whether *cis/trans* isomerisation is a *prerequisite* for the branching reaction, as it occurs to a significant level at the reaction temperature even in the absence of any catalyst (exp. 10 to 12). In the presence of the commercial ferrierite, the OA/EA equilibrium is reached much more rapidly, and is not rate-limiting in the branching reaction. However, under the slow stirring conditions employed in this work, mass transfer of the reactant to the external active site is probably overall rate-limiting. Starting with EA, a high concentration of the preferred isomeric form is directly available for entry to the pore mouths, and therefore the observed activity is higher—furthermore, bulky by-products resulting from external surface reactions (estolides and dimerised acids) are formed in lower amount, resulting in a higher BUFA yield.

Spent catalyst characterisation

In order to further confirm the pore-mouth hypothesis, the spent zeolite materials have been studied using a combination of three micro-spectroscopy methods.

Micro-spectroscopy of the powdered FER catalysts

Deactivation of the reference powdered catalysts under similar reaction conditions has already been studied in detail.^[18] The UV/Vis bulk diffuse reflectance (DR) spectroscopy of spent powdered catalysts (powder 1) showed at least two types of carbonaceous deposits to be present: enlylic carbocations (absorbing at 290, 355–360, 440–445 and 500–650 nm) and aromatic species (at 410–420 and 480–490 nm). The intensities of all absorption bands attributed to the enlylic species decreased with reaction time, while those associated with the aromatic species increased.

In this work, the same spent powder samples have been analysed by visible micro-spectroscopy (in DR mode). The visible spectra shown in Figure 4a are characterised by the same absorption bands above 400 nm with similar intensity trends, so that their assignment can be directly transposed. Next, these spent powder samples have been investigated by wide-field fluorescence, in order to confirm the fluorescent properties of the carbonaceous deposits, and (when possible) to optimise the excitation light to target certain specific species. Figures 4b and c show the changes in fluorescence as a function of excitation light and reaction time (0.5 and 6 h) for the catalyst particles (crystal agglomerates). Based on the visible absorption data, light between 400–440 nm excites aromatic species (those with absorption at 415 nm, but also those with ab-

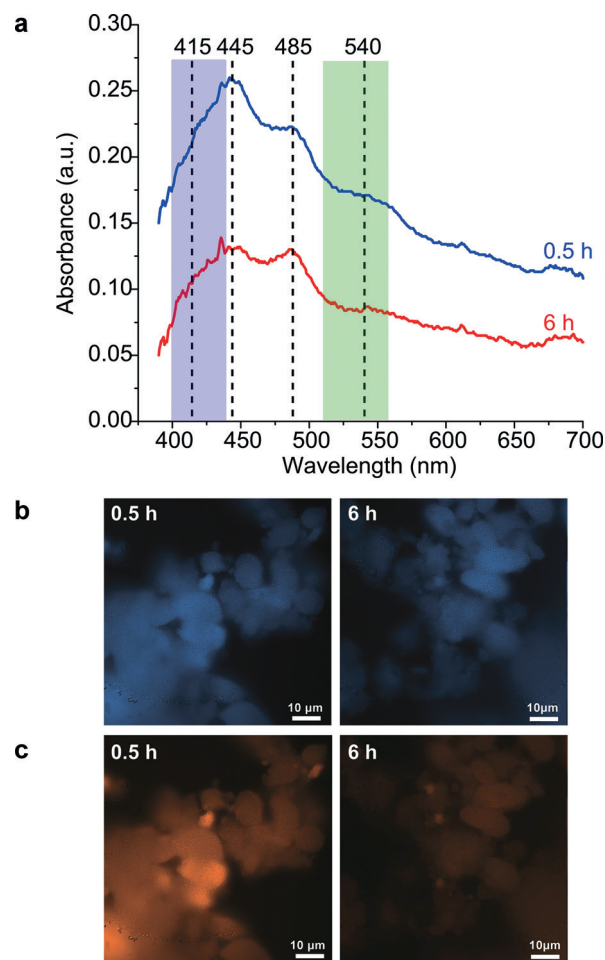


Figure 4. a) Visible micro-spectroscopy spectra of two spent powder ferrierite samples (powder 1) collected after performing alkyl isomerisation of OA (260 °C, 5.0 wt.% loading, 0.5 and 6 h);^[18] the bands (shoulders) at 445 and 540 nm are assigned to enlylic carbocations, while those at 415 and 485 nm are attributed to aromatic species; the two light excitation ranges (400–440 nm and 510–560 nm) used in the wide-field fluorescence experiments are highlighted in the visible micro-spectroscopy spectra. b, c) Wide-field fluorescence micro-spectroscopy images recorded for the same two spent powder ferrierite samples (powder 1); b) images were obtained after light excitation at 400–440 nm (emission above 470 nm); c) images were recorded after excitation at 510–560 nm (emission above 590 nm); the scale bars represent 10 μm.

sorption at 480–490 nm) and trienlylic carbocations (with absorption at 445 nm).

The fluorescence level hardly varies between 0.5 and 6 h. Since the aromatic species are formed at an early stage of the reaction, while the enlylic carbocation concentration decreases with OA conversion,^[18] the aromatic species must dominate the fluorescence signal. When switching to excitation light between 510–560 nm, the fluorescence originates from more conjugated systems which, based on the visible micro-spectroscopy work, are tentatively attributed to tetraenlylic carbocations absorbing at about 540 nm. While the formation of such cations requires successive hydrogen transfer reactions and their concentration must therefore be low, detection of these carbocations is aided by the high fluorescence sensitivity to such species. The fluorescence level is significant at the begin-

ning of the reaction, and then decreases after 6 h. This decreasing intensity also confirms that the fluorescence level is not significantly affected by any aromatic species, at least during the first 6 h of the reaction. This is perhaps surprising, because the characteristic absorption band (480–490 nm) of these aromatics is intense and relatively close to the excitation range; however, if they had contributed significantly to the fluorescence, their intensity would be expected to remain constant with reaction time, contrary to what is actually observed.

Building up a spatial distribution from intensity and density of fluorescent points, the 3D image (Figure 5a) clearly shows some disparities at this early stage of the reaction. As discussed above, aromatic species are mainly responsible for the fluorescence in the range 495–545 nm and are already present on a large number of particles; polyenylic carbocations (detected by their fluorescence in the range 550–600 nm) seem concentrated on certain agglomerates, independently of the agglomerate size. Based on earlier investigations,^[18] the aromatics are believed to block the channels and the polyenylic species to poison the acid sites. These results therefore suggest large

differences in acidity between particles (with respect to accessibility and/or strength), for the powder ferrierite.

Taken together, the data mentioned above show that the aromatic and polyenylic cationic species have distinct fluorescent properties, which allow the use of (confocal) fluorescence microscopy to precisely locate the carbonaceous deposits formed on the zeolite during alkyl isomerisation.

Micro-spectroscopy of large FER crystals

The spent powdered samples discussed above served as reference for the DR visible micro-spectroscopy analysis of the spent large model ferrierite crystals collected from experiments 7–9. The thin platelets are grey with darker edges (Figure 6a) and the exfoliated ones are darkened mainly at the edges (Figure 6b); in some cases, brown patches can also be seen close to the middle. A number of crystals from each type were studied, focusing on spectral differences between edges (both along Y and Z) and the rest of the basal surface YZ. Each visible spectrum collects information from a cross-section of about

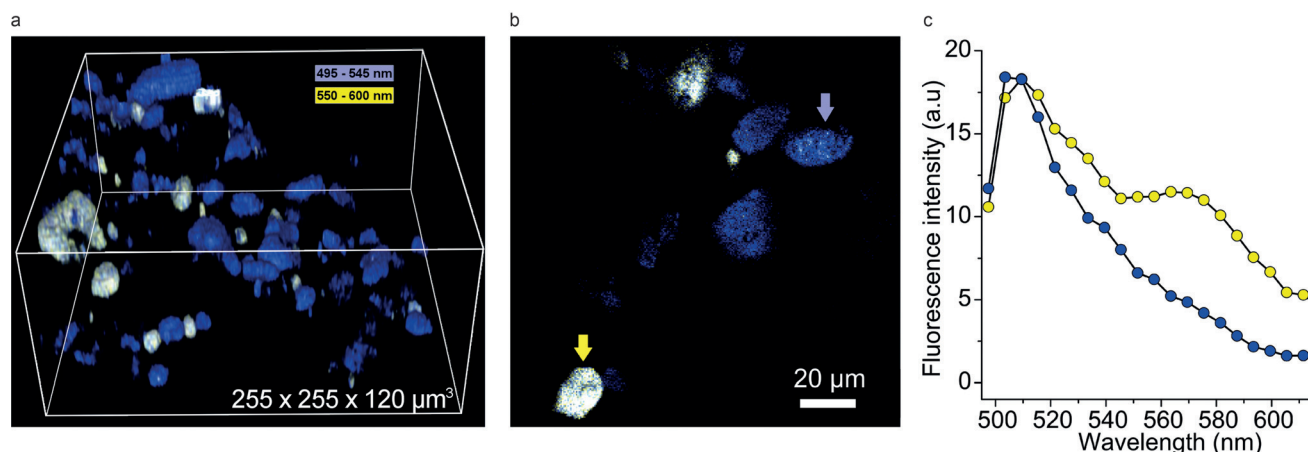


Figure 5. Confocal fluorescence micro-spectroscopy images of spent powder ferrierite (powder 1) collected after alkyl isomerisation of OA (260 °C, 0.5 h, 5.0 wt. % loading).^[18] a) 3D fluorescence image of the catalyst particles after laser-light excitation at 488 nm; the image is colour-coded in blue for the 495–545 nm emission and in yellow for the 550–600 nm emission; the dimensions of the volume under study are 255 × 255 × 120 μm³. b) 2D confocal fluorescence image indicating the lateral distribution of fluorescence. c) Fluorescence spectra recorded for two typical particles marked with the blue and yellow arrows in (b), using the same colour coding.

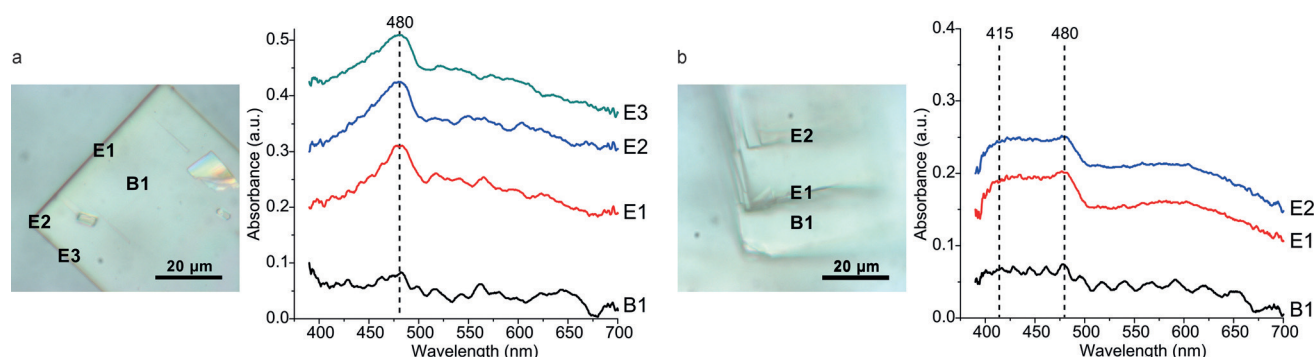


Figure 6. Visible micro-spectroscopy image and spectra recorded for: a) a flat H-FER spent crystal collected from experiment 7 (OA reactant with 1.0 wt. % crystals loading, 260 °C, 96.5 h); b) for an exfoliated H-FER spent crystal collected from experiment 9 (distilled EA reactant with 2.0 wt. % crystals loading, 260 °C, 96.5 h); each image shows the position of the sampling points, where the visible spectra have been recorded (i.e., edges vs. basal planes of the large H-FER spent crystals); the bands at 415 and 485 nm are attributed to aromatic species.

5 μm^2 . As expected, the spectra recorded from most fresh crystals do not show any absorption (data not shown).

Absorption spectra recorded at the edges of a spent flat platelet from experiment 7 (OA, 1.0 wt.% crystals, Figures 6a) are characterised by a distinct band at 480–485 nm associated with aromatic species. Its intensity is somewhat stronger along the width edge (Y, E1) and at the corner E2 than along the length edges (Z, E3). Bands related to the enylic carbocations (440–445 nm) cannot be clearly seen. Importantly, visible spectra recorded at spots on the basal surface far removed from the edges do not show any light absorption (B1). A spent exfoliated model crystal collected from experiment 9 (distilled EA, 2.0 wt.% crystals, Figure 6b) shows similar features, with all edge spectra characterised by the 480–485 nm band (E1–E2) and those recorded in the step between two edges without any absorption (e.g. B1). In addition, a broad absorption band between 415 and 480 nm can be seen in the spectra recorded at the edges. This suggests the presence of trienylic carbocations and/or aromatic species absorbing at 415 nm.

The visible method allows a first mapping of the carbonaceous deposits that are apparently located only at the edges of the spent large model crystals. Width (Y) and length (Z) edges are characterised by similar visible spectra and therefore host the same carbonaceous species. This is surprising, since it suggests that they are produced equally in the 10-MR channel openings (Y edges) and the 8-MR channel openings (Z edges), despite their significant size difference; this is later explained from the fluorescence microscopy after excitation with polarised light.

By comparison with the visible analysis of the reference ferrierite powder 1, these carbonaceous species must include alkyl aromatics. Determination of the monoenylic and dienylic carbocations (absorbing below 400 nm) is not possible with visible microscopy, and the detection of tri- and other polyenylic species is hindered by their very low level.

In addition to visible micro-spectroscopy, polarised confocal fluorescence micro-spectroscopy has been applied in order to gain further spatial resolution, and to attempt to discriminate between the role of the 10-MR and 8-MR channels. The excitation light wavelength was first checked using flat spent crystals from experiment 9 (distilled EA, 2.0 wt.% crystals), as this run

did show traces of the BUFA product. To understand whether the catalyst activity plays any role in the “coking” process, images were also recorded for flat spent crystals from experiment 8 (non-distilled EA, 1.0 wt.% crystals), in which conversion was much lower. The influence of double bond configuration (EA instead of OA), and crystal type (exfoliated vs. flat), are illustrated with data obtained for a spent exfoliated crystal collected from experiment 7 (OA, 1.0 wt.% crystals).

Figures 7a and b show the confocal fluorescence micro-spectroscopy 2D images recorded for a flat spent model crystal from experiment 9 (distilled EA, 2.0 wt.% crystals), for laser excitation at 488 and 561 nm (a and b, respectively). The micro-spectroscopy visible spectra recorded for the spent powder catalyst (powder 1, Figure 4) and the spent model crystals (Figure 6) are used to help assignment of the carbonaceous species responsible for the observed fluorescence with the flat spent model crystal from experiment 9. Results obtained with the spent large crystals are similar to those observed with the spent reference powders: excitation with light of 488 nm (Figure 7a) seems optimum, as the aromatic species absorb at 480–485 nm, again giving the image with the highest fluorescence intensity. Polyenylic carbocations are excited by a 561 nm laser (Figure 7b), although their measured intensity is weak due to their very low concentration. The high sensitivity of the fluorescence method for such species, and its approach from the low energy end of the spectrum, helps to detect them while minimising interference from the aromatics that absorb at lower wavelengths.

In both cases (Figure 7a and b), the fluorescent species are clearly restricted to the edges. Interestingly, the fluorescent edges of the width (which house the pore mouths of the 10-MR channels) seem more intense than those of the length (which house the pore mouths of the 8-MR channels). Similar observations can be made when switching feedstock to OA (data not shown). The images delivered by this method for the flat crystal are consistent with the mapping recorded from the visible absorption microscopy.

Additionally, Figure 7 shows the 2D (c) and 3D (d) fluorescence microscopy images of a flat spent model crystal from experiment 8 (non-distilled EA, 1.0 wt.% crystals) after excitation at 561 nm. The results show that already at lower conversion

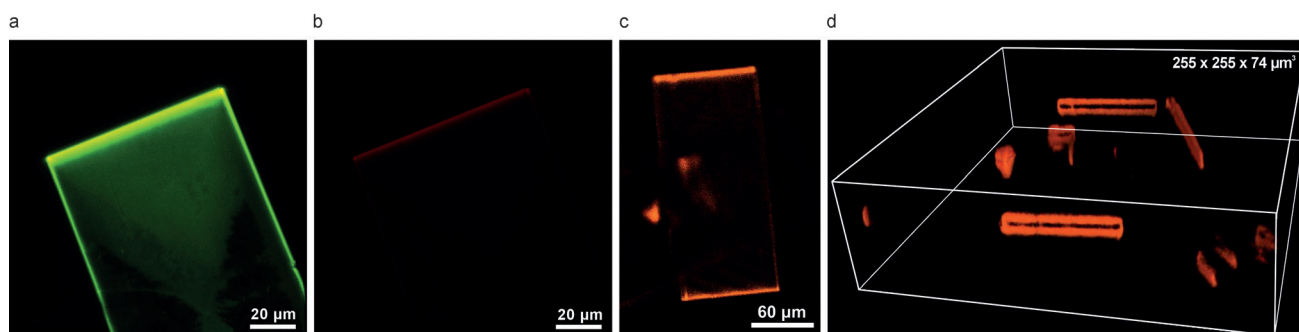


Figure 7. a, b) 2D confocal fluorescence micro-spectroscopy images recorded for a flat spent model H-FER crystal collected from experiment 9 (distilled EA reactant with 2.0 wt.% crystals loading, 260 °C, 96.5 h) following laser light excitation at: a) 488 nm, and b) 561 nm; similar laser power and collection time have been used to allow direct comparison. c, d) Confocal fluorescence micro-spectroscopy images in 2D (c) and 3D (d) recorded for a flat spent model H-FER crystal collected from experiment 8 (non-distilled EA reactant with 1.0 wt.% crystals loading, 260 °C, 96.5 h) following laser light excitation at 561 nm; laser power has been increased to enable visualisation of the fluorescent carbonaceous species; the dimensions of the volume under study are 255 × 255 × 74 μm^3 .

(compared to experiment 9), the deposits (and therefore the reaction) are already restricted to the very edges of the width cross section. The 3D image pinpoints the precise location as the width edge corners, the central area of the width cross-section being free from deposits. This is a surprising finding, as “coke” may be expected to cover the complete (10-MR) edge area in a uniform layer. The inhomogeneous deposition observed seems too distinct and regular to be explained solely by the easier approach of the bulky reactant molecules to these exposed edges, and/or the more favourable location for growth of the larger carbonaceous species. We postulate that the distinct hollowing of the width of the crystals, as evidenced by closer inspection of the SEM images, is the result of preferential desiccation (by the NaOH post-treatment/cleaning) and that this inhomogeneity of the width structure is the reason for the distinct localisation of the fluorescence.

The distribution of the carbonaceous deposits at the very edges of the crystal has been studied in more detail. Figure 8 shows wide-field fluorescence micro-spectroscopy 2D images following excitation at 510–560 nm recorded for the flat spent model crystal from experiment 8 (non-distilled EA, 1.0 wt.% crystals), the same crystal imaged in Figures 7c and d. Based on the visible adsorption and fluorescence results presented earlier for the spent powder catalyst (powder 1), the fluorescence is tentatively attributed to the polyenylic carbocations. When polarisation is parallel to the crystal length (Figure 8b), light is clearly emitted from most edges, with a thicker and more homogeneous fluorescent band at the width edges. For this platelet crystal, the thickness of the fluorescent width edges is estimated at about 5 μm , while the thickness of the length edges is estimated at about 3 μm (Figure 8c). Again, emission is especially strong at the corners, and is also visible at a crack in the crystal. However, when rotating the crystal by 90° (Figure 8a), the edges can no longer be seen, while a small crystal (piece) with a perpendicular orientation appears via the fluorescence of its edges (as indicated by the arrow in Fig-

ure 8a). This result confirms the transition dipole moment orientation of the fluorescent species along the crystal length, and therefore along the 10-MR channels. Fluorescence along the two length edges cannot be explained by “coking” of the 8-MR channel openings; these are perpendicular to the polarisation and their diameter seems too small to allow a perpendicular orientation of the fluorescent molecules there, knowing that these species are already constrained in the larger 10-MR channels. The two fluorescence bands are also too thick (well above 500 nm) to be attributed to a monolayer of molecules at the pore mouths. Therefore, the fluorescence must originate from the 10-MR channels running along the length edges.

Similar conclusions can be drawn for the exfoliated spent model crystals. Figure 9 shows a 2D image obtained by polarised confocal fluorescence micro-spectroscopy after excitation at 488 nm (aromatic species) for a specific exfoliated crystal from experiment 9 (distilled EA, 2.0 wt.% crystals). Its crossed structure allows direct visualisation of the light polarisation effect. Figure 9a clearly shows the light emitted by all edges from the bottom substructure with the length parallel to the polarisation, while the edges from the perpendicular top substructure are not visible. When rotating the crystal by 90° (Figure 9b), the edges of the top substructure become visible through their fluorescence, while those of the bottom one disappear.

This clearly confirms the orientation of the aromatic species along the length and the 10-MR channels.

The presence of carbonaceous species exclusively in the 10-MR channels is in line with one of the conclusions from our recent study of the relationship between ferrierite acidity and performance in five commercial catalysts; initial pore conversion was found to correlate with the concentration of Brønsted acid sites in the 10-MR channels, as determined by adsorption/desorption of pyridine and FT-IR.^[49] With the 10-MR extremities occupied and blocked by the “coke” species, the observed fluorescence distribution is clearly consistent with the alkyl iso-

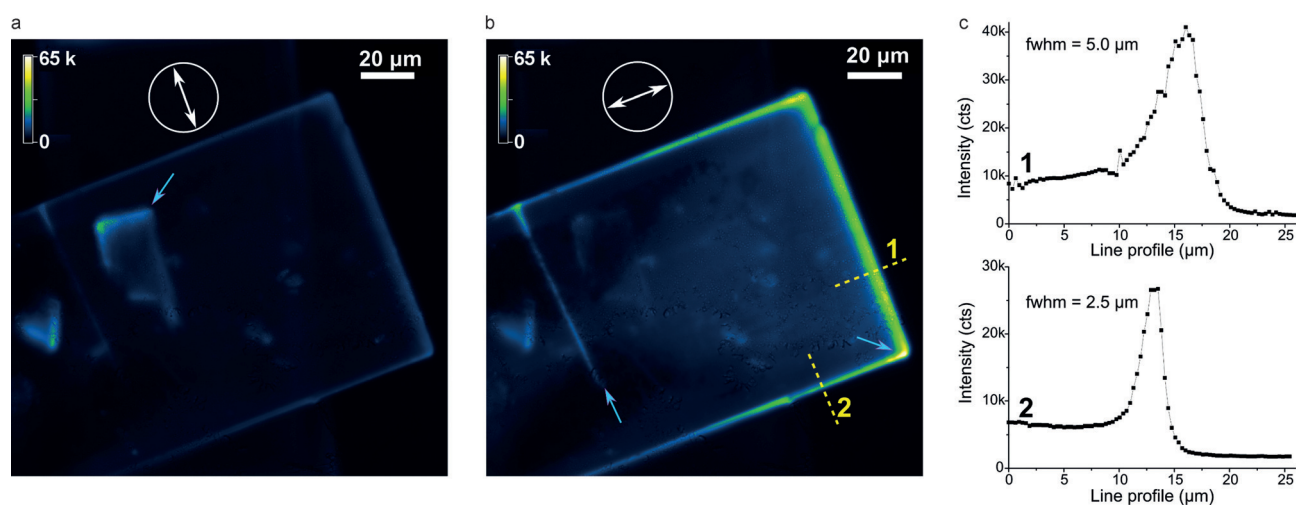


Figure 8. Polarised 2D wide-field fluorescence micro-spectroscopy images recorded for a flat spent model H-FER crystal collected from experiment 8 (non-distilled EA reactant with 1.0 wt.% crystals loading, 260 °C, 96.5 h) following light excitation at 510–560 nm (emission above 590 nm); the excitation light was polarised, as indicated by the double arrows, along the 8-MR channels (image a) and along the 10-MR channels (image b). The graphs (c) show the estimation of the fluorescence thickness of the width edge and the length edge, curves 1 and 2 respectively.

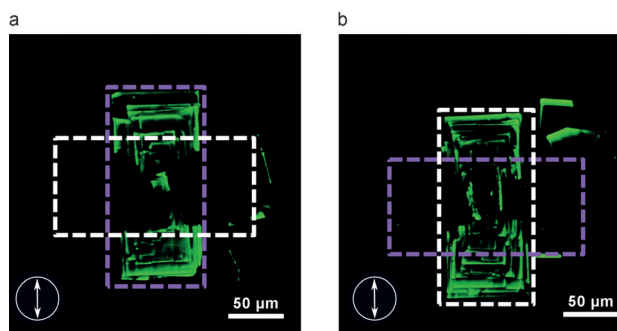


Figure 9. Polarised 2D wide-field fluorescence micro-spectroscopy images recorded for a crossed exfoliated spent model H-FER crystal collected from experiment 9 (distilled EA reactant with 2.0 wt. % crystals loading, 260 °C, 96.5 h) following laser light excitation at 488 nm. In the image a, only the bottom part of the crystal (highlighted with purple dashes), where the 10-MR channels are aligned along the (laser) polarised light, is visible through the fluorescence of the carbonaceous species; after rotation by 90° of the sample support, the image b shows exclusively the top part of the crystal (highlighted with white dashes).

merisation reaction being restricted to the pore entrance, and therefore further supporting the pore mouth catalysis hypothesis. Additional evidence comes from our earlier observation that pore blockage occurs at the very beginning of the reaction (as soon as the reaction temperature is reached).^[18]

The restriction of carbonaceous species to the very edges of the crystal is different from earlier findings reported for H-ZSM-5 in the conversion of alcohols to olefins, where a gradual coking from the edges to the centre has been observed.^[31] With SAPO-34 on the other hand, the narrow windows characteristic of the CHA framework block the formation of carbonaceous deposits at the edges of the crystal, resulting in rapid deactivation of the catalyst;^[31] this mode of coke formation and deactivation is somewhat closer to that seen in H-FER. Although the pore size of the studied ferrierite catalysts is optimal for the alkyl isomerisation reaction, their crystal morphology is far from ideal, as only the pore mouths of the 10-MR channels at the width cross-section are actively employed in the catalysis. Reduction of the crystal size has the expected effect of increasing the activity of the catalyst, simply by increasing the (10-MR) pore mouth concentration per unit volume/mass; in the study above, we estimate a factor of approximately 50–250 times when comparing the reference commercial ferrierites to the model crystals. Further optimisation of the morphology could, for instance, be focused on the synthesis of thin, platelet-like crystals in which the 10-MR channels run perpendicular to the basal plane. In a related study, Roberts et al. investigated the alkyl isomerisation of unsaturated fatty acids using zeolite types omega (MAZ), mordenite (MOR) and L (LTL); they similarly confirmed the importance of the crystal morphology to reactivity and selectivity, and proposed a minimum crystallite diameter to depth ratio of 10.^[53,54]

Conclusions

The liquid-phase skeletal isomerisation of OA and EA has been carried out over large ferrierite model crystals. A combination

of visible and polarised confocal fluorescence microscopy has been applied to the spent catalyst materials in order to gain insights—at the single particle level—into the deactivation mechanisms, and to provide support to the earlier proposed concept of pore mouth catalysis.

SEM has confirmed the integrity of the model catalyst after activation and reaction under the selected conditions. Two types of large H-FER crystals are identified, namely thin and exfoliated zeolite platelets. Despite their very low non-basal surface area and pore mouth density, careful selection of the reaction conditions (i.e., slow stirring and long reaction time) enabled the catalysis of geometrical, positional and (to a minor extent) alkyl isomerisation.

Comparison of the catalytic results obtained for the model catalyst and the commercial powdered zeolite ferrierite materials, shows that the large crystals are indeed valid models for the study of catalyst deactivation during the skeletal alkyl isomerisation of OA. The importance of crystal size (and thus number of pore mouths per unit mass) on catalyst activity and BUFA yields is already evidence of the pore mouth catalysis.

The spent zeolite catalyst materials have subsequently been studied by a combination of microscopy and micro-spectroscopy techniques. Using visible micro-spectroscopy, aromatic species could be identified in the model catalysts. Traces of more conjugated species, such as polyenylic carbocations, are suggested by fluorescence microscopy. The presence of both species is shown to be independent of double bond configuration (OA or EA) and crystal type.

With respect to the spatial mapping, visible microscopy shows the same aromatic species at most edges of the spent large model crystals, once again independently of crystal type and feedstock. The spatial resolution of the (confocal) fluorescence micro-spectroscopy confirms that all carbonaceous deposits are located at most edges in both thin and exfoliated zeolite platelets, as well as at a number of fissures in flat crystals. In addition, polarisation of the excitation light has revealed their presence exclusively in the 10-MR channels: close to the opening of the 10-MR channels, these deposits result in complete blockage, while the absence of “coke” species deeper in the 10-MR channels confirms that access has been prevented. Deposits found at the length edges suggest that some coking of the 10-MR channels also runs along these edges; we hypothesise that this is due to imperfections in the external 10-MR channel wall, created either during manufacture or due to attrition in the reaction.

In conclusion, the investigation of spent large ferrierite crystals after skeletal isomerisation of OA and EA provides further experimental evidence for the existence of pore mouth catalysis in H-FER materials. Our study confirms that only a very limited number of acid sites are accessible to the reactant, despite the ideal pore size and acidity of ferrierite for this reaction. Therefore, activity could be further enhanced by better catalyst design, opening up the potential for an effective and economically viable catalytic route to selective alkyl branching of natural lipid materials.

Experimental Section

Chemicals and catalyst material

OA (tradename Priolene 6936; composition: 92.2% C18:1, 3.2% C18:2, 0.2 C18:3 and 3.7% saturated fatty acids (mainly octadecanoic acid)) was obtained from Croda. Elaidic acid (EA, >98%) was purchased from ABCR. The EA was found to have a high content of Na⁺ and K⁺ (total 100 mg kg⁻¹), which was reduced by distillation to 5 mg kg⁻¹ (ICP-MS). The OA contained less than 1 mg kg⁻¹ Na⁺ and K⁺.

The different ferrierite samples used are listed in Table 1. The reference K⁺-ferrierite (powder 1) was activated by conversion to its protonated form, further denoted as H-FER, using an ion-exchange procedure with hydrochloric acid (HCl, 1 M) at room temperature (RT),^[55] before air drying the material for three days at RT. The reference NH₄⁺-ferrierite (powder 2) was calcined for 5 h at 500 °C. The model crystal catalyst ICT-10^[46,47] had been treated after synthesis with sodium hydroxide (NaOH, 0.1 M) to remove any EFAI and therefore it had to be reactivated by multiple wet ion exchange (4 times NH₄NO₃, 0.5 M) and 5 h calcination at 500 °C (heating at 4 °C min⁻¹). NH₄NO₃ (>99%) was purchased from Merck.

Catalytic testing

Testing of the model catalyst required the use of a small-volume reactor, and some adaptation of the reaction conditions, compared to the standards used for the commercial catalyst powder 1.^[18] All reactions were carried out with 1.0 or 2.0 wt.% H-FER loading on OA in a 10 mL swagelok reactor, starting with the following amounts: 4.5 g OA or EA and 49.0 μL demineralised water. After heating to 260 °C (resulting in a calculated pressure of 7.15 bar) the reaction temperature was typically held for 96.5 h, while tumbling (6 rpm), before the reactors were cooled to 50 °C and their content directly filtered using a syringe filter (PTFE, 0.20 μm). The experiments, consisting of a combination of gentle tumbling together with very long reaction time (8–16 times longer than in ref. [18]) were designed such that the conversion with the model catalyst was enhanced, while preserving its integrity as much as possible.

Because of the large differences in molecular weight of the components in the crude reaction mixture, its composition was determined in two steps. First, the oligomer concentration in the crude reaction mixture was determined by high temperature GC (HT-GC). Secondly, the monomeric fraction was separated from the oligomers by distillation at a temperature of 260 °C under a pressure of <1 mbar. Subsequently, to reduce chemical complexity and facilitate analyses, a small amount of the collected monomeric fraction was diluted in ethyl acetate (40 mg mL⁻¹), hydrogenated at RT for 45 min using 40 mg Adam's catalyst (reduced in situ, hydrogen flow of 50 mL min⁻¹) and subjected to GC analyses.

OA (with an initial mass fraction $x_{C18:1,0}$), linoleic acid ($x_{C18:2,0}$) and linolenic acid ($x_{C18:3,0}$), are considered as the reactive components of OA; positional and *cis/trans* isomers are implicitly included in the simplified nomenclature. Their mass conversion (y_t) was determined by quantification of the mass fraction of stearic acid ($x_{C18,t}$) in the hydrogenated monomer fraction as a function of time, t . The onset of the reaction ($t=0$) is designated as the time when the reaction mixture reaches the temperature set-point of 260 °C. A correction is made for the distillation yield of the monomeric species ($y_{M,t}$) as determined by HT-GC, and for the initial mass fraction of unreactive species, that is, the amount of stearic acid ($x_{C18,0}$) present in OA. The mass conversion of all unsaturated compo-

nents, subsequently referred to simply as "conversion", is then given by:

$$y_t = 1 - \frac{[(x_{C18,t} + x_{C18:1,t}) \times y_{M,t} - x_{C18,0}]}{[x_{C18:1,0} + x_{18:2,0} + x_{C18:3,0}]} \quad (1)$$

Note that due to the similar molecular weights of these molecules, mole and mass conversions can be considered almost equivalent. The selectivity towards BUFA ($s_{B,t}$) is derived from the mass fraction of all hydrogenated BUFA ($x_{B,t}$) in the hydrogenated monomer fraction. Again, a correction was made for the distillation yield of the monomeric species ($y_{M,t}$):

$$s_{B,t} = \frac{[x_{B,t} \times y_{M,t}]}{[(x_{C18:1,0} + x_{18:2,0} + x_{C18:3,0}) \times y_t]} \quad (2)$$

The composition of the crude reaction mixtures was determined using high-temperature GC (HT-GC) after methylation using diazomethane. The GC was equipped with a cold on-column injection and a metal column with a nonpolar stationary phase Cp-SimDist Ultimet (Chrompack WCOT, 5 m × 0.53 mm × 0.17 μm) and the components detected with a flame ionisation detector (FID) based on retention time. The carrier gas was He with a constant flow of 20 mL min⁻¹. The temperature program used was: initial temperature of 60 °C, hold for 1 min; temperature increase of 30 °C min⁻¹ until 150 °C; hold 0 min; temperature increase of 12 °C min⁻¹ until 380 °C; hold 10 min. The detector was set at 400 °C. The injection volume was 1 μL for a concentration of 1 mg mL⁻¹.

The hydrogenated monomer fractions were analysed by GC after methylation with diazomethane. The GC was equipped with a split injection and a fused silica capillary column with a polar stationary phase FFAP-CB (Chrompack WCOT, 25 m × 0.32 mm × 0.30 μm), and the components detected with FID based on retention time. The carrier gas was He with a constant flow of 2.1 mL min⁻¹ and a split flow of 75 mL min⁻¹. The temperature program used was: initial temperature of 120 °C, hold for 0 min; temperature increase of 8 °C min⁻¹ until 250 °C; hold 20 min. The detector was set at 270 °C. The injection volume was 1 μL for a concentration of 40 mg mL⁻¹.

For GC-MS identification, the crude mixtures were dissolved in heptane and the components separated by HT-GC. The GC was equipped with a cold on-column injection and a capillary column with a nonpolar stationary phase ZB-1HT (Zebtron Inferno, 30 m × 0.32 mm × 0.1 μm). The carrier gas was He with a constant flow rate of 2.5 mL min⁻¹. The temperature program used was: initial temperature of 50 °C, hold for 1 min; temperature increase of 15 °C min⁻¹ until 400 °C; hold 20 min. The injection volume was 0.5 μL. The components were detected with a quadrupole MS detector (Agilent MSD 5975 B Inert) in electron ionisation mode (70 eV). The interface temperature was set at 350 °C, the source temperature at 230 °C and the quadrupole temperature at 150 °C. The scan range was 29–1050 amu with 1.48 scans s⁻¹. The samples were analysed directly and after hydrogenation and methylation with diazomethane.

For the *cis/trans* determination, the monomeric fractions were analysed by GC after methylation with diazomethane. The GC was equipped with a split injection and a fused silica capillary column with a highly polar stationary phase CP Sil 88 (Agilent 25 m × 0.32 mm × 0.20 μm), and the components detected by FID based on retention time. The carrier gas was He with a constant flow of 1.41 mL min⁻¹ and a split flow of 141 mL min⁻¹. The temperature program used was: initial temperature of 160 °C, hold for 10 min.

The detector was set at 275 °C. The injection volume was 1 µL for a concentration of 10 mg mL⁻¹.

Catalyst characterisation

Scanning electron microscopy: The scanning electron microscopy (SEM) images were recorded using a FEI XL30SFEG microscope, after sputtering with Pt/10% Pd.

UV/Vis micro-spectroscopy: The set-up is based on an Olympus BX41 upright microscope working in reflectance mode, equipped with a 50× 0.5 NA high working-distance microscope objective lens. A 75 W tungsten lamp was used for illumination. Reflected light was directed to a CCD video camera (ColorView IIIu, Soft Imaging System GmbH) via a 50/50 double viewport tube, and to a UV/Vis spectrometer (AvaSpec-2048TEC, Avantes BV) via a 200 µm core fibre.

Fluorescence microscopy: The fluorescence microscopy measurements were carried out using an upright Nikon Eclipse 90i confocal fluorescence microscope, equipped with a 50× 0.55 NA dry objective lens. Both wide-field illumination and confocal scanning modes were used for imaging. For wide-field fluorescence experiments, excitation light was provided by a Xe arc lamp. Fluorescence light was collected in reflectance mode with an EMCCD camera (QuantEM: 5125C). Two filter cubes were used to control the excitation and emission ranges: 1) BV-2A filter cube with an excitation pass band 400–440 nm, a 455 nm dichroic mirror and a long pass emission filter at 470 nm; 2) G-2A filter cube with an excitation pass band 510–560 nm, 575 nm dichroic mirror and a long pass emission filter at 590 nm. A rotatable polariser was used to selectively polarise the excitation light in order to yield the maximum and minimum of fluorescence emission. Confocal fluorescence images were recorded using excitation from two laser light sources (488 and 561 nm) connected to a Nikon-Eclipse A1R scanning head equipped with corresponding dichroic mirrors to reject the excitation light. The emission light was detected in the range of (400–750 nm) by using a spectral detection unit equipped with a diffraction grating and a 32 photomultiplier tube array.

Acknowledgements

The authors thank Croda for financial support. V.R.R.M., J.K. and J.W. acknowledge financial support of this project by the German Science Foundation (DFG). We would also like to thank Marjan Versluijs-Helder (Utrecht University, UU) for performing the SEM analyses, while Marjolein Velthoen and Suzanne Verkleij (UU) are thanked for helping with the visible micro-spectroscopy. Negar Rashidi, Marvin Burger and Stephan Langelaar (Croda) contributed to this work by carrying out a number of syntheses and analyses.

Keywords: ferrierite · isomerisation · micro-spectroscopy · pore mouth catalysis · zeolites

- [1] F. R. Ribeiro, F. Alvarez, C. Henriques, F. Lemos, J. M. Lopes, M. F. Ribeiro, *J. Mol. Catal. A* **1995**, *96*, 245–270.
- [2] J. P. Gilson, E. G. Derouane, *J. Catal.* **1984**, *88*, 538–541.
- [3] T. F. Degnan, *J. Catal.* **2003**, *216*, 32–46.
- [4] S. Ernst, R. Kumar, J. Weitkamp, *Catal. Today* **1988**, *3*, 1–10.
- [5] S. Ernst, J. Weitkamp, J. A. Martens, P. A. Jacobs, *Appl. Catal.* **1989**, *48*, 137–148.
- [6] M. C. Claude, J. A. Martens, *J. Catal.* **2000**, *190*, 39–48.

- [7] J. A. Munoz Arroyo, G. G. Martens, G. F. Froment, G. B. Marin, P. A. Jacobs, J. A. Martens, *Appl. Catal. A* **2000**, *192*, 9–22.
- [8] J. A. Martens, G. Vanbutsele, P. A. Jacobs, J. F. M. Denayer, R. Ocackoglu, G. Baron, J. A. M. Arroyo, J. W. Thybaut, G. B. Marin, *Catal. Today* **2001**, *65*, 111–116.
- [9] M. C. Claude, G. Vanbutsele, J. A. Martens, *J. Catal.* **2001**, *203*, 213–231.
- [10] W. Huybrechts, G. Vanbutsele, K. J. Houthoofd, F. Bertinchamps, C. S. L. Narasimhan, E. M. Gaigneaux, J. W. Thybaut, G. B. Marin, J. F. M. Denayer, G. V. Baron, P. A. Jacobs, J. A. Martens, *Catal. Lett.* **2005**, *100*, 235–242.
- [11] T. L. M. Maesen, M. Schenk, T. J. H. Vlugt, J. P. de Jonge, B. Smit, *J. Catal.* **1999**, *188*, 403–412.
- [12] G. Sastre, A. Chica, A. Corma, *J. Catal.* **2000**, *195*, 227–236.
- [13] T. L. M. Maesen, R. Krishna, J. M. van Baten, B. Smit, S. Calero, J. M. Castillo Sanchez, *J. Catal.* **2008**, *256*, 95–107.
- [14] P. Andy, N. S. Gnep, M. Guisnet, E. Benazzi, C. Traversy, *J. Catal.* **1998**, *173*, 322–332.
- [15] S. van Donk, J. H. Bitter, K. P. de Jong, *Appl. Catal. A* **2001**, *212*, 97–116.
- [16] F. C. Meunier, L. Domokos, K. Seshan, J. A. Lercher, *J. Catal.* **2002**, *211*, 366–378.
- [17] S.-H. Lee, C.-H. Shin, S. B. Hong, *J. Catal.* **2004**, *223*, 200–211.
- [18] S. C. C. Wiedemann, J. A. Stewart, F. Soulimani, T. van Bergen-Brenkman, S. Langelaar, B. Wels, P. de Peinder, P. C. A. Bruijninx, B. M. Weckhuysen, *J. Catal.* **2014**, *316*, 24–35.
- [19] H. L. Ngo, R. O. Dunn, E. Hoh, *Eur. J. Lipid Sci. Technol.* **2012**, *114*, 213–221.
- [20] C. Scrimgeour, in *Bailey's Industrial Oil and Fat Products*, 6th ed. (Eds.: F. Shahidi), Wiley, Hoboken, **2005**, pp. 1–43.
- [21] T. A. Isbell, R. Kleiman, B. A. Plattner, *J. Am. Oil Chem. Soc.* **1994**, *71*, 169–174.
- [22] B. M. Weckhuysen, *Angew. Chem. Int. Ed.* **2009**, *48*, 4910–4943; *Angew. Chem.* **2009**, *121*, 5008–5043.
- [23] A. M. Beale, S. D. M. Jacques, B. M. Weckhuysen, *Chem. Soc. Rev.* **2010**, *39*, 4656–4672.
- [24] M. H. F. Kox, K. F. Domke, J. P. R. Day, G. Rago, E. Stavitski, M. Bonn, B. M. Weckhuysen, *Angew. Chem. Int. Ed.* **2009**, *48*, 8990–8994; *Angew. Chem.* **2009**, *121*, 9152–9156.
- [25] G. De Cremer, B. F. Sels, D. E. De Vos, J. Hofkens, M. B. J. Roeffaers, *Chem. Soc. Rev.* **2010**, *39*, 4703–4717.
- [26] K. P. F. Janssen, G. De Cremer, R. K. Neely, A. V. Kubarev, J. van Loon, J. A. Martens, D. E. De Vos, M. B. J. Roeffaers, J. Hofkens, *Chem. Soc. Rev.* **2014**, *43*, 990–1006.
- [27] R. A. Schoonheydt, *Chem. Soc. Rev.* **2010**, *39*, 5051–5066.
- [28] E. Stavitski, B. M. Weckhuysen, *Chem. Soc. Rev.* **2010**, *39*, 4615–4625.
- [29] C. Chmelik, J. Kärger, *Chem. Soc. Rev.* **2010**, *39*, 4864–4884.
- [30] J. Kärger, T. Binder, C. Chmelik, F. Hibbe, H. Krautscheid, R. Krisna, J. Weitkamp, *Nat. Mater.* **2014**, *13*, 333–343.
- [31] D. Mores, E. Stavitski, M. H. F. Kox, J. Kornatowski, U. Olsbye, B. M. Weckhuysen, *Chem. Eur. J.* **2008**, *14*, 11320–11327.
- [32] D. Mores, J. Kornatowski, U. Olsbye, B. M. Weckhuysen, *Chem. Eur. J.* **2011**, *17*, 2874–2884.
- [33] J. P. Hofmann, D. Mores, L. R. Aramburo, S. Teketel, M. Rohn, J. Janek, U. Olsbye, B. M. Weckhuysen, *Chem. Eur. J.* **2013**, *19*, 8533–8542.
- [34] Q. Qian, J. Ruiz-Martinez, M. Mokhtar, A. M. Asiri, S. A. Al-Thabaiti, S. N. Basahel, B. M. Weckhuysen, *Catal. Today* **2014**, *226*, 14–24.
- [35] Q. Qian, J. Ruiz-Martinez, M. Mokhtar, A. M. Asiri, S. A. Al-Thabaiti, S. N. Basahel, B. M. Weckhuysen, *ChemCatChem* **2014**, *6*, 772–783.
- [36] A. N. Parvulescu, D. Mores, E. Stavitski, C. M. Teodorescu, P. C. A. Bruijninx, J. M. K. Gebbink, B. M. Weckhuysen, *J. Am. Chem. Soc.* **2010**, *132*, 10429–10439.
- [37] I. L. C. Buurmans, B. M. Weckhuysen, *Nat. Chem.* **2012**, *4*, 873–886.
- [38] L. R. Aramburo, E. de Smit, B. Arstad, M. M. van Schooneveld, L. Sommer, A. Juhin, T. Yokosawa, H. W. Zandbergen, U. Olsbye, F. M. F. de Groot, B. M. Weckhuysen, *Angew. Chem. Int. Ed.* **2012**, *51*, 3616–3619; *Angew. Chem.* **2012**, *124*, 3676–3679.
- [39] L. R. Aramburo, J. Ruiz-Martinez, L. Sommer, B. Arstad, R. Buitrago-Sierra, A. Sepúlveda-Escribano, H. W. Zandbergen, U. Olsbye, F. M. F. de Groot, B. M. Weckhuysen, *ChemCatChem* **2013**, *5*, 1386–1394.
- [40] L. R. Aramburo, S. Teketel, S. Svelle, S. R. Bare, B. Arstad, H. W. Zandbergen, U. Olsbye, F. M. F. de Groot, B. M. Weckhuysen, *J. Catal.* **2013**, *307*, 185–193.

- [41] M. H. F. Kox, E. Stavitski, B. M. Weckhuysen, *Angew. Chem. Int. Ed.* **2007**, *46*, 3652–3655; *Angew. Chem.* **2007**, *119*, 3726–3729.
- [42] C. Sprung, B. M. Weckhuysen, *J. Am. Chem. Soc.* **2015**, *137*, 1916–1928.
- [43] A. Kuperman, S. Nadimi, S. Oliver, G. A. Ozin, J. M. Garcés, M. M. Olken, *Nature* **1993**, *365*, 239–242.
- [44] R. E. Morris, S. J. Weigel, *Chem. Soc. Rev.* **1997**, *26*, 309–317.
- [45] J. Kärger, P. Kortunov, S. Vasenkov, L. Heinke, D. B. Shah, R. A. Rakoczy, Y. Traa, J. Weitkamp, *Angew. Chem. Int. Ed.* **2006**, *45*, 7846–7849; *Angew. Chem.* **2006**, *118*, 8010–8013.
- [46] V. R. R. Marthala, M. Hunger, F. Kettner, H. Krautscheid, C. Chmelik, J. Kärger, J. Weitkamp, *Chem. Mater.* **2011**, *23*, 2521–2528.
- [47] F. Hibbe, V. R. R. Marthala, C. Chmelik, J. Weitkamp, J. Kärger, *J. Chem. Phys.* **2011**, *135*, 184201.
- [48] P. A. Vaughan, *Acta Crystallogr.* **1966**, *21*, 983–990.
- [49] S. C. C. Wiedemann, A. Muñoz-Murillo, R. Oord, T. van Bergen-Brenkman, B. Wels, P. C. A. Bruijninx, B. M. Weckhuysen, *J. Catal.* **2015**, *329*, 195–205.
- [50] H. L. Ngo, A. Nunez, W. Lin, T. A. Foglia, *Eur. J. Lipid Sci. Technol.* **2007**, *109*, 214–224.
- [51] J. Datka, M. Kawalek, K. Góra-Marek, *Appl. Catal. A* **2003**, *243*, 293–299.
- [52] A. Philippaerts, S. Paulussen, S. Turner, O. Lebedev, G. Van Tendeloo, H. Poelman, M. Bulut, F. De Clippel, P. Smeets, B. Sels, P. Jacobs, *J. Catal.* **2010**, *270*, 172–184.
- [53] W. R. Hodgson, C. M. Lok, G. Roberts, W. T. Koetsier, European patent 0774451 B1, to Unichema Chemie B.V, **1997**.
- [54] W. R. Hodgson, W. T. Koetsier, C. M. Lok, G. Roberts, US patent 5856539, to Unichema Chemie B.V, **1999**.
- [55] R. Rachwalik, Z. Olejniczak, B. Sulikowski, *Catal. Today* **2005**, *101*, 147–154.

Received: September 5, 2015

Published online on November 27, 2015